Battery-free, wireless, cuff-type, multimodal physical sensor for continuous temperature and strain monitoring of nerve

Seunghwan Kim[1†], Yong Suk Oh[1†], Kwanghyoung Lee[2], Seongchan Kim[3], Woo-Youl Maeng[4], Kyung Su Kim[4], Ga-Been Kim[3,4], Seokjoo Cho[1], Hyeonseok Han[1], Hyunwoo Park[5], Mengqiu Wang[6,7], Raudel Avila[6,7], Zhaoqian Xie[6,7], Kabseok Ko[8], Jungrak Choi[1], Minkyu Je[5], Hyojin Lee[3], Sungho Lee[2], Jahyun Koo[4,9], Inkyu Park[1]**

† These authors contributed equally to this work.

Seunghwan Kim, Yong Suk Oh, Seokjoo Cho, Hyeonseok Han, Jungrak Choi, Inkyu Park
Department of Mechanical Engineering
Korea Advanced Institute of Science and Technology
Daejeon 34141, Republic of Korea
E-mail: jahyunkoo@korea.ac.kr and inkyu@kaist.ac.kr.

Kwanghyoung Lee, Sungho Lee
Department of Thoracic and Cardiovascular Surgery
Korea University College of Medicine
Seoul 02841, Republic of Korea.

Seongchan Kim, Ga-Been Kim, Hyojin Lee
Center for Biomaterials
Korea Institute of Science and Technology
Seoul 02841, Republic of Korea.

Woo-Youl Maeng, Kyung Su Kim, Ga-Been Kim
School of Biomedical Engineering
Korea University
Seoul 02841, Republic of Korea.

Hyunwoo Park, Minkyu Je
School of Electrical Engineering
Korea Advanced Institute of Science and Technology
Daejeon 34141, Republic of Korea

Mengqiu Wang, Raudel Avila, Zhaoqian Xie
State Key Laboratory of Structural Analysis for Industrial Equipment
Department of Engineering Mechanics
Dalian University of Technology
Dalian 116023, P.R.China

Mengqiu Wang, Raudel Avila, Zhaoqian Xie
Ningbo Institute of Dalian University of Technology
Ningbo 315016, P.R.China

Kabseok Ko
Qualcomm Institute
La Jolla, CA 92093, USA

Keywords: battery-free, wireless, strain sensor, temperature sensor, nerve

Peripheral nerve injuries cause various disabilities related to loss of motor and sensory functions. The treatment of these injuries typically requires surgical operations for improving functional recovery of nerve. However, capabilities for continuous nerve monitoring remains a challenge. Herein, we introduce a battery-free, wireless, cuff-type, implantable, multimodal physical sensing platform for continuous *in vivo* monitoring of temperature and strain from the injured nerve. The thin, soft temperature and strain sensors wrapped around the nerve exhibit good sensitivity, excellent stability, high linearity, and minimum hysteresis in relevant ranges. In particular, the strain sensor integrated with circuits for temperature compensation provides reliable, accurate strain monitoring with negligible temperature dependence. The system enables power harvesting and data communication to wireless, multiple implanted devices wrapped around the nerve. Experimental evaluations, verified by numerical simulations, with animal tests demonstrate the feasibility and stability of the sensor system, which have great potential for continuous *in vivo* nerve monitoring from an early stage to complete regeneration.

1. Introduction

Twenty million Americans suffer from peripheral nerve injuries (PNIs), which are mainly generated by accidental trauma or repetitive compression in daily life and cost $150 billion annually for treatment. [1,2] The effects on patients include motor and sensory deficits, which require surgical treatment for functional recovery and regeneration of the injured nerve. [3] However, failure to achieve complete functional recovery due to delayed regeneration and long nerve gap injuries leads to irreversible degeneration of the end organ (*e.g.*, motor unit) within 12-18 months after denervation. [4,5] Previous reports suggest that more than 30% of the patients experience incomplete and/or poor recovery after the surgical treatment, causing a permanent physical disability near the repaired nerve. [6] Accurate measurement of physical or physiological signals from the injured nerve also can provide great possibility for appropriate assessment and immediate treatment criteria of functional recovery along with understanding nerve generation mechanism and guiding medical protocols (Supplementary Note1). Conventional methods for measuring the physiological signals include H_2 polarography [7–10], laser Doppler flowmetry [11], and histological analyses [12–17], which can elucidate changes in blood flow (or dynamics) in the injured nerve. However, these techniques have several disadvantages, including being complicated and time-consuming, requiring highly trained technicians, and inducing secondary damages to the nerve by measurement. In addition, the intraoperative approaches could not support continuous, real-time, and long-term operations, essentially required for practical use in neuromonitoring applications. A few studies propose an

impedance analysis based on soft electrodes for continuous monitoring of physiological signals. [18,19] However, the electrical measurement of the impedance includes many unwanted signals arising from wound fluid, electrode contact, and corrosion of the exposed electrodes for long-term monitoring. This electrophysiological evaluation has limitation in distinguishing axon damage and nerve amputation. As an alternative approach, measurement of anatomic changes in the nerve, including diameter, cross-sectional area, and modulus (fat content) supports a quantitative basis for evaluation of nerve injuries and regeneration. [20] Especially, severe nerve defects (>5 mm) in humans that yields high tension coaptation resulting in reduced Schwann cell activation and ischemia [21,22] should be treated carefully in end-to-end suturing [23,24] with a strain sensor.

Recent advances in technologies for a soft, thin, and implantable sensor capable of continuously measuring physical parameters (*i.e.*blood flow, strain, pressure, temperature, pH *etc.*) [25–28] have great potential for continuous *in vivo* nerve monitoring. In addition, an integration of wireless platforms (e.g., a bluetooth low energy (BLE[28]) or a near field communication (NFC[29])) with these devices supports untethered, real-time monitoring by wirelessly power supply and data communication for use in a variety of implantable medical applications. However, the BLE platform includes bulky batteries and percutaneous wire, which prevent free motions and increases stress and anxiety of the animals due to physical constraints. [30,31] In this context, the NFC platform is one of the most promising strategies with resolving these drawbacks. The battery-free operation based on a resonant magnetic inductive coupling to harvest power makes the implantable device smaller and more comfortable for subjects.[32] The wireless communication between the implantable device and an external reader allows for freedom of movement and reduces the risk of infection due to the percutaneous wire. In addition, this approach can provide capabilities for continuous *in vivo* nerve monitoring along with not only therapies for improving regeneration, including wireless electrical, optogenetic, and pharmacologic stimuli [33–35], but also neuropathic pain treatment using local cooling. [27,36]

Toward this objective, this paper introduces a battery-free, wireless, implantable, multimodal physical (BWIMP) sensing platform for continuous *in vivo* monitoring of the injured nerve, as an initiative for the abovementioned technology. The thin, soft, fully implantable, cuff-type, wireless sensor wrapped around the nerves can provide continuous measurement of temperature and strain with conformal contact to the surface of nerve. To the best of our knowledge, this is the first study on the integration of multiple physical sensors into an implantable medical device for neuromonitoring applications. In particular, both temperature and strain sensing features exhibit excellent signal stability and high linearity without hysteresis and drift in the relevant

ranges (body temperature < 40 °C, strain < 10 %). The incorporation of specific geometrical and electrical designs of multimodal sensors enables the independent discrimination of multiple stimuli without mutual interference. A battery-free, wireless device configuration can provide the entire system to be light, simple, and completely implantable without hampering free motions. Continuous *in vivo* measurement of temperature and strain for injured nerve demonstrates the feasibility, biocompatibility, and stability of the sensor system. The BWIMP sensing platform could provide great potential for the development of advanced therapeutic protocols and clinical paradigms in the neuromedical field (Figure S1), via wireless and implantable monitoring of abnormal nerve regeneration (*e.g.*, blood flow interruption: ischemia, nerve expansion: excessive scar tissue, and nerve shrinkage: demylination) in the post-surgery state during prolonged periods.2. Results and Discussions

2.1. Design of the battery-free, wireless, implantable, multimodal physical sensing platform

Figure 1A presents a promising concept of continuous temperature and strain measurement utilizing a BWIMP sensing platform that consists of two parts: (i) thin, cuff-type sensors gently wrapped around a peripheral nerve for continuous *in vivo* monitoring of the temperature and strain of the nerve; and (ii) a battery-free, wireless platform for power transfer and data communication with a primary antenna and a near field communication (NFC) reader located outside the body. The multimodal physical sensors include a temperature sensor and a strain sensor connected to a battery-free, wireless platform for continuous capture of both the temperature and strain arising from blood flow and volume change of the peripheral nerve, respectively. Figure 1B shows a schematic illustration of the response of the BWIMP sensing platform to temperature and strain stimuli. This BWIMP sensing platform can independently measure changes in temperature and strain due to the blood flow inside the nerve and volume expansion of the nerve without mutual interference.

Figure 1C shows an exploded view schematic illustration of the overall assembly design and constituent materials of the BWIMP sensing platform that meet appropriate requirements, including reasonable sensitivity, high linearity, low hysteresis, and long-term stability for the *in vivo* nerve monitoring application considered here. The multimodal physical sensors utilize a tri-layered film that includes an Au membrane (thickness = 50 nm) on a neutral plane and polyimide (PI) films (total thickness = 5 μm) on the top and bottom layers, encapsulated by a thin, soft elastomer film (Ecoflex 0030, total thickness = 100 μm, Smooth-On, Inc.). The tri-layered film (PI/Au/PI) includes a temperature sensor, a strain sensor, and serpentine

interconnects, which depend on the patterning of the Au membrane and etching of the PI film. The PI films protect the Au membrane from excessive mechanical deformation. The thin, soft encapsulation film enables conformal wrapping around the peripheral nerve with minimal physical restriction of natural behavior of the nerve as its elastic modulus (*E* of Ecoflex 0030 < 70 kPa) is lower than those of typical peripheral nerves of the mammals (*E* greater than several hundred kPa), as shown in Figure S2. [37,38] All components used in the multimodal physical sensors exhibit non-toxic properties, biocompatibility, and chemical stability [39,40], which are essential features in the context of the applications envisioned here. Figure S3 and "Fabrication of cuff-type, multimodal physical sensors" in the Materials and Methods section provide the detailed fabrication procedure and key materials. Microfabrication processes (*e.g.*, photolithography and reactive ion etching) and a stamping transfer method using water-soluble tape enable the excellent reproducibility of the thin, soft tri-layered film with sophisticated and microscale patterns. In the battery-free, wireless platform, an NFC System on a Chip (SoC) consists of a spiral-shaped receiver loop antenna, an NFC chip (RF430FRL154H, Texas Instruments), two amplifiers (INA333, Texas Instruments), and additional electronic components bonded to integrated circuits (ICs) on a flexible printed circuit board (FPCB) (Au/PI/Au/PI, thickness = 20 μm/50 μm/20 μm/50 μm). Encapsulation layers (Ecoflex 0030, white color, thickness = 1 mm) protect the NFC SoC from external damage and provide mechanical/electrical barriers to biofluids from infiltrating the electrical system. This battery-free, wireless sensing platform using the NFC protocol enables the fabrication of lightweight devices with the thinnest, smallest, and most flexible forms for fully implantable, long-term operation of such devices interfaced to the surfaces of vital, living organs for *in vivo* clinical trials. A flexible flat connector (FFC) serves as a link for the electrical connection between the electrodes of the sensors and the NFC SoC.

Figure 1D-F provide photographs of the fabricated multimodal physical sensors (width = 4 mm; total length = 35 mm; thickness = 100 μm) that consist of a sensor array part and an electrode part, as shown in Figure 1D. In Figure 1E, the sensor array part, directly in contact with peripheral nerve, exhibits stretchability owing to not only the intrinsically elastic properties of the encapsulation layer, but also the geographical stretchability of the serpentine interconnects. The length of the electrode part ranged from of 10 mm to 30 mm depending on the interior spaces of various subject animals (Figure S4). Figure 1F presents that the soft, thin film layout of the sensors ensures conformal contact against curved surfaces of a commercial tube with a diameter of 1 mm, similar to the typical diameters of the peripheral nerves of the target animals (*e.g.* rats and rabbits). Figure 1G shows a cross-sectional scanning electron microscopy (SEM)

image of the tri-layered film. The Au traces are located in proximity of neutral plane of the stacked tri-layered film to reduce its bending stresses [41] Figure 1H and I show a photograph of the prepared NFC SoC platform and a schematic diagram of an equivalent LC circuit corresponding to the loop antenna, sensor-ICs, and NFC-ICs built on the FPCB. Figure 1J presents a photograph of the fabricated BWIMP sensing platform.

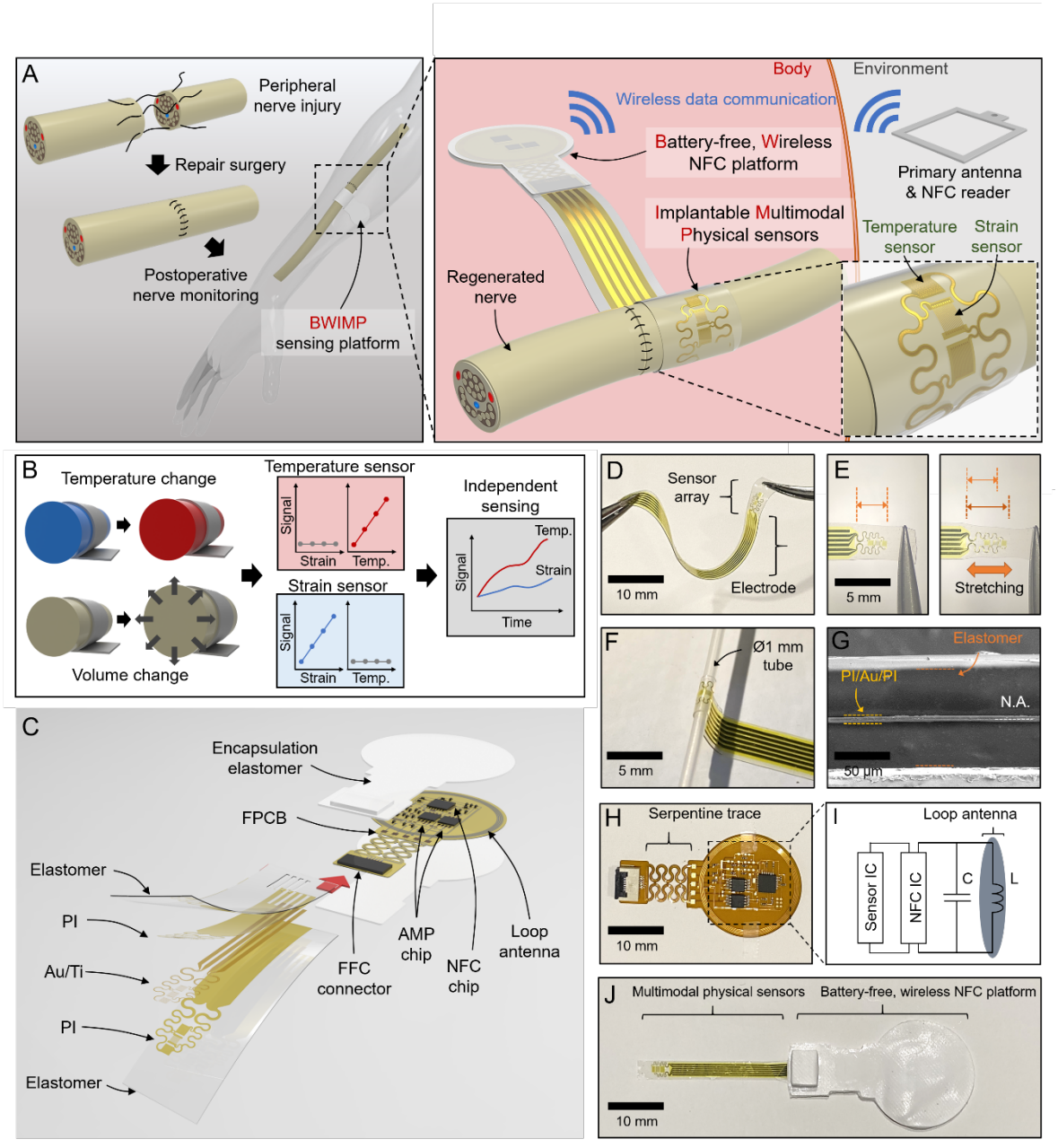

Figure 1. Battery-free, wireless, implantable, multimodal physical (BWIMP) sensing platform for continuous *in vivo* nerve monitoring. (A) Schematic illustration of the concept of the proposed postoperative nerve monitoring using a BWIMP sensing platform after repair surgeries of injured peripheral nerves. The sensing device composed of cuff-type implantable multimodal physical sensors and a battery-free, wireless NFC platform is wrapped around a regenerated nerve inside the body. It detects multiple physical states (temperature and strain)

of the nerves and wirelessly transfers the measured data to outside the body. (B) Independent and simultaneous sensing of changes in the temperature and strain arising from blood flow and/or diameter changes in the nerve without mutual signal interference. (C) Schematic illustration of the overall design of the sensing device with an exploded view. Integration of the cuff-type sensor having a multi-encapsulated thin film structure (Ecoflex/PI/Au/PI/Ecoflex, Ecoflex, thickness = 100 μm; PI, thickness = 5 μm; Au, thickness = 50 nm) and the NFC platform where electric components (NFC chip, AMP chip, *etc.*) are built on a FPCB, which yields the BWIMP sensing platform after packaging by encapsulation elastomers. (D) Photograph of the fabricated cuff-type sensors. (E) Photographs comparing normal and stretched configurations, presenting a locally stretched sensor array part. (F) Photograph of the sensor surrounding a commercial tube with an outer diameter of 1 mm. (G) SEM image of a cross-sectional view in which the PI/Au/PI layer is located at the neutral axis of the stacked structure. (H) Photograph of the fabricated NFC SoC. (I) Schematic diagram of an equivalent electrical circuit on the FPCB for wireless data communication. (J) Photograph of the fabricated BWIMP sensing platform.

2.2. Design for sensing/decoupling of temperature and strain signals

In general, temperature and strain sensors based on metal membranes incorporated by a single encapsulation film are sensitive to both temperature and strain stimuli. To separate the responses to temperature and strain stimuli, the BWIMP sensing platform involves the following two design strategies: (i) discriminated geometry between the temperature and strain sensors to achieve different strain-sensitivities depending on the form factors of metal traces and PI films and (ii) an electrical circuit with a Wheatstone bridge using a dummy strain sensor for temperature-compensation of the strain sensor. Figure 2A provides microscopic images of a temperature sensor, an active strain sensor, a compensating dummy strain sensor, and serpentine interconnects connecting each sensor and electrodes. Each sensor exploits Au traces (linewidth = 5 μm) across an area of 500 × 500 μm^2, which is a small portion of the entire area. As shown in Figure S5, the 3D finite element analysis (FEA) results reveal that the sensor structure applies little constraint on the surface beneath the sensors even under stretching (ε_y = 10%) owing to its compliant property. The magnified microscopic images in Figure 2B clearly compare the sizes and shapes of the Au and PI films in each sensor. Figure 2B (i) shows Au traces (width 5 μm) patterned with a half-and-half Peano serpentine layout, which undergo similar insensitivity to strain along both the X and Y axes. [42] These Au traces embedded into a non-patterned PI film (square shape, width 500 μm; length 500 μm) prevent the temperature

sensor from being easily deformed by external forces, minimizing the electrical resistance change (ΔR_T) under tensile stresses. Figure 2B (ii) and (iv) present an Au trace (width 5 μm) patterned with a typical metal strain gauge layout and etching of the PI film (width 10 μm) along these metal lines, which enables the high sensitivity to strain (*i.e.*, gauge factor). This design provides high deformability, increasing the fractional change in the resistance of the strain sensor (ΔR_a) at the same strain stimulus compared with that of the temperature sensor. The 3D FEA results in Figure 2C (i) and (ii) clearly exhibit the difference in the strain distribution on the patterned Au traces for the temperature sensor and active strain sensor under 10% stretching along the Y- axis. In addition, the plot in Figure 2C (iv) compares the maximum strain values ($\varepsilon_{Au,max}$ = 0.1% for the temperature sensor; $\varepsilon_{Au,max}$ = 1.2% for the active strain sensor). 3D FEA results in Figure S6 confirm the prevention of excessive deformation of the tri-layered film due to absorption of local strain by the surrounding elastomer near the interface between the two regions ($\varepsilon_{elastomer}$ = 30 %). The maximum strain values on the Au trace linearly increase with an external strain of 15% and are still below the fracture strain of Au ($\varepsilon_{Au,fracture}$ = 2-2.5 % [43,44]) for both the temperature sensor and the active strain sensor, leading to mechanical reliability even under high strain, as verified by the experimental results presenting different gauge factor (GF) in the strain-response curves in Figure S7.

Figure 2D and E summarize the sensing performance of the temperature sensor. Figure 2D clearly shows the differences in the responses of the temperature sensor to temperature and strain stimuli. The response to temperature exhibits high linearity (R^2 = 0.99) with a temperature-sensitivity (S_T) of 0.22 %°C^{-1}, negligible hysteresis between the heating and cooling with almost perfectly reversible response (< 2%). In contrast, the response to strain is negligible (under ε < 10%), enabling accurate and stable temperature sensing without interference from strain. The temperature sensor shows a change of 2.2% ($\Delta R_T/R_T$) under a temperature change of 10 °C, whereas it experiences only a change of 0.035% ($\Delta R_T/R_T$) under an applied strain of 10%. Figure 2E depicts the instant response of the temperature sensor to the temperature stimulus by a water droplet falling, as shown in Figure S8A. This rapid response (8°C/s) arises from fast heat conduction and small heat capacity due to the thin film-type sensor (thickness = 100 μm). The continuous responses at different temperature change (ΔT=0, 1, and 2 °C) shows in Figure S8B present reasonable resolution with high SNR (signal to noise ratio) of 100.

On the other hand, the active strain sensor exhibits responses to both strain and temperature owing to the temperature dependence of Au, as shown in Figure S9. This effect can be removed using the Wheatstone bridge for temperature compensation containing the active strain sensor

and a dummy strain sensor [45], as shown in Figure 2F. The base resistance of the dummy strain sensor (R_d) is the same as that of the active strain sensor (R_a) as the shape of the Au trace is the same, whereas it is insensitive to the external strain owing to the embedding of the Au trace onto a non-patterned PI film. Figure 2B (iii) and 2C (iii) present the microscope image and the FEA result of the Au trace embedded onto a non-patterned PI film in the dummy strain sensor. Figure S10 illustrates the method and principle of temperature-compensation using the Wheatstone bridge in more detail.

Figure 2G-K summarize the sensing performance of the temperature-compensated (T-C) strain sensor. Figure 2G compares the responses of the T-C strain sensor to strain and temperature stimuli. The strain sensor shows a change of 0.6 mV in voltage under an applied strain of 10%, whereas it exhibits only a change of ±0.005 mV in voltage under a temperature change of 10 °C (Figure S11), clearly showing decoupled strain-sensing property. These results exhibit significantly enhanced temperature-independence due to the aforementioned design approach, as shown in Figure S12. Figure 2H illustrates the responses to cyclic loading at strain levels of 2%, 4%, 6%, 8%, and 10%, presenting significantly low hysteresis (< 3%) over the entire strain range with reversible loading/unloading and complete recovery of the original states with high linearity (R^2 = 0.99). Figure 2I shows the responses to loading-holding-unloading cycles at strain levels of 0.1%-1% and 1%-10%, showing accurate distinction of the different strains with a resolution of less than 0.2%. As shown in Figure 2J, the measured response time, defined as the difference between the 90% rising times ($\Delta\tau_{90\%}$) of the sensor signal (blue curve) and the input strain (red curve), is 50 ms at the step loading of 5 % strain. These results indicate that the T-C strain sensor can instantly respond to input loads without a substantial delay. Figure 2K exhibits excellent mechanical/electrical reliability and high repeatability under 500 cyclic loadings with a strain of 10% without structural failure or signal instability. In particular, the baseline of the signal remains constant after 1, 100, and 400 cyclic loadings, indicating that the T-C strain sensor is insensitive to changes in environmental condition unlike the active strain sensor, as shown in Figure S13.

Figure 2L and M present the stability of the cuff-type, implantable, multimodal physical sensors wrapped around the tube. Figure 2L compares the changes in the fractional resistance at different bending radii (r) from 0.75 mm to 2.5 mm, revealing that the change is less than 0.03%. These results indicate that each sensor exhibits no change in fractional resistance regardless of the value of r. Furthermore, the sensor should show long-term stability in *in vivo* environments. Figure 2M demonstrates the stability of sensor after the immersion in phosphate-buffered saline

(PBS) solution for 3 weeks. These results indicate that the biofluid cannot penetrate into the sensor owing to the complete encapsulation of the sensor with Ecoflex.

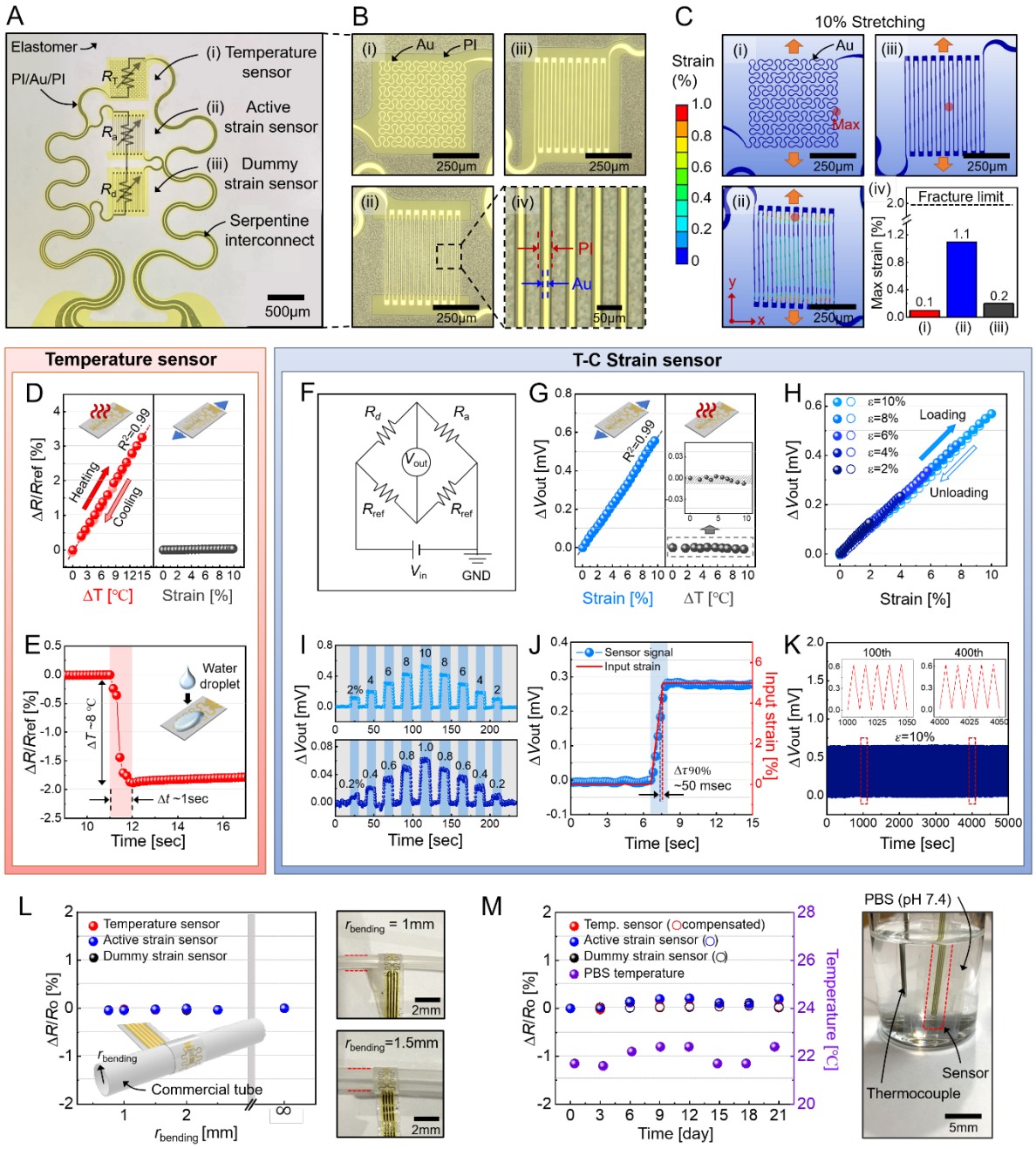

Figure 2. Design strategy and performance characterization of a multimodal physical sensor. (A) Microscopic image of the sensor array part composed of (i) a temperature sensor, (ii) an active strain sensor, (iii) a dummy strain sensor, and serpentine interconnects. (B) Magnified microscopic images of the detailed geometries. (C) FEA results of the strain distribution on the Au membrane of the sensors under stretching (ε_y = 10%). (D) Temperature- and strain-response curves of the temperature sensor (under ΔT of 0-15 °C and ε of 0-10%). (E) Transient response of the temperature sensor under a rapid temperature stimulus (ΔT of 8 °C for 1s) due to water droplets on the sensor. (F) Schematic diagram of an electrical circuit for temperature-

compensation of the strain sensing, where the active and dummy strain sensors constitute a Wheatstone bridge circuit. (G) Strain- and temperature-response curves of a temperature-compensated (T-C) strain sensor (under ΔT of 0- 10 °C and ε of 0-10%). The inset shows an enlarged version of the temperature-response curve of the T-C strain sensor. (H) Hysteresis characteristics under loading-unloading cycles for applied strains of 2%, 4%, 6%, 8%, and 10%. (I) Dynamic response of the T-C strain sensor for various strain inputs ($0.2\% < \varepsilon < 10\ \%$) with a strain rate of 5 %/s. (J) Transient response of the T-C strain sensor under step loading comparing the sensor signal (blue color) and input strain (red color) with a $\Delta\tau_{90\%}$ of 50 ms. (K) Cyclic responses of the T-C strain sensor under 500 repetitive loading-unloading cycles with an applied strain of 10%. The insets present the signals at the 100^{th} and 400^{th} cycles. (L) Fractional resistance changes of the sensors at different radii of curvature of the interfacial surfaces and photographs of the sensor on cylindrical commercial tubes with radii of 1 mm and 1.5 mm. (M) Fractional resistance changes of the sensors under long-term immersion in PBS (pH 7.4) for three weeks and associated photograph.

2.3. Battery-free, wireless measurement system

Figure 3A and S14A show a schematic illustration and photograph of a battery-free, wireless sensing system for continuous measurement of temperature and strain using the BWIMP sensing platform, respectively. This system consists of an NFC reader, a primary antenna, and a portable computer to provide power delivery and data communication with the battery-free, wireless sensing platform wrapped around the nerve of a subject animal on a customized surgery table. In Figure S14B, the primary antenna integrated with a rod supports capability to rotate and/or move in the X, Y, and Z directions freely, depending on the location and height of the nerve related to the species and/or the size of the subject animal. Figure 3B shows the equivalent electrical circuit of the overall measurement system. Figure S15 illustrates the detailed electrical circuit built into the BWIMP sensing platform, which includes a Wheatstone bridge for temperature sensor, a Wheatstone bridge for the temperature compensation using active and dummy strain sensors, and the NFC chips connected to the receiver antenna. Figure S16 provides a detailed block diagram of the wireless temperature and strain sensing processes. The NFC reader and primary antenna transfer power to the NFC chip through the receiver antenna using resonant magnetic inductive coupling, which drives the sensor-integrated circuit (IC) for the readout of data from the temperature and strain sensors. Wheatstone bridges convert the change in resistance (ΔR) of the temperature and strain sensors into changes in voltage (ΔV), respectively. The ΔV signals measured from the temperature and T-C strain sensors passes the

343 instrumentation amplifier to amplify the signal to improve the signal quality. The internal
344 analog-to-digital converter (ADC) in the NFC SoC converts the voltage signals obtained from
345 the temperature sensor and T-C strain sensor into digital signals. Finally, the NFC SoC converts
346 the digital signals into a data format that conforms to the ISO 15693 protocol and transfers the
347 data to the NFC reader. The application software, developed using Python, supports continuous
348 monitoring and visualization of the collected data from the temperature and strain sensors. This
349 device yields real-time readings of temperature and strain in a fast (a sampling rate < 10 Hz),
350 sequential readout scheme, which is sufficient for the postoperative nerve monitoring. Figure
351 3C shows the simulation results of the magnetic field distribution, direction, and strength for
352 the single primary antenna in the X-Z plane, exhibiting symmetrical properties with respect to
353 the X axis. As shown in Figure 3D, the wireless data communication within the X-Y plane (30
354 cm × 30 cm) can operate over a maximum height (Z_{max}) of 17 cm at the center and 13 cm at the
355 edge, where Z is the distance from the sensing device to the primary antenna. This result
356 indicates that the measurement system supports stable operation over a long distance of 13 cm,
357 which typically depends on the antenna diameter, size, and power. Furthermore, evaluation of
358 the stability of the measurement system involves specific events that could occur during actual
359 nerve monitoring, including (i) tweezer manipulation and (ii) movement of the sensing device.
360 Figure 3E and F reveal negligible fluctuations in the voltage signals measured from both the
361 temperature sensor and T-C strain sensors, even under the repeated approach of the tweezers
362 and the lateral movement of the sensing device by 5 cm, respectively.
363

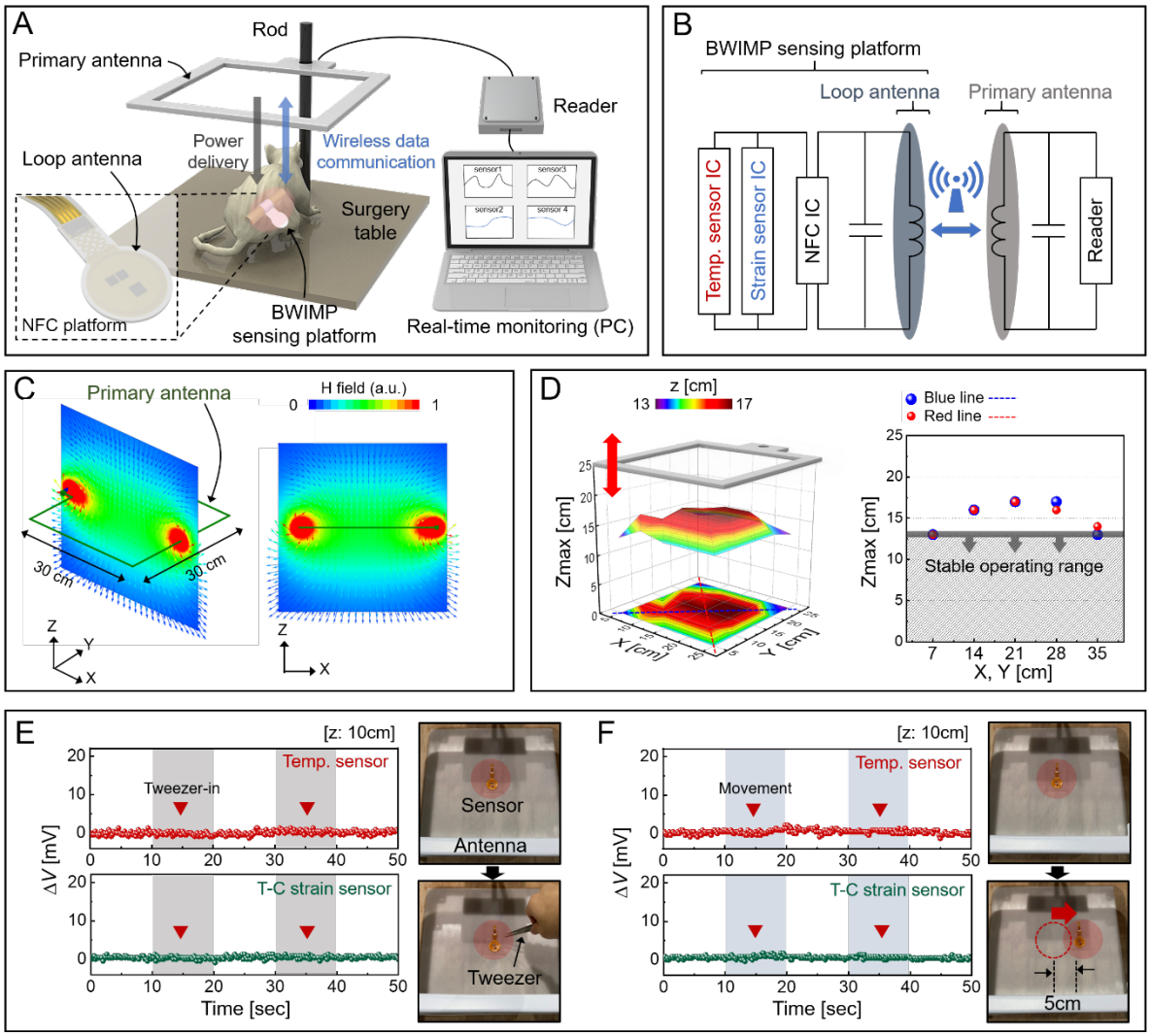

Figure 3. Battery-free, wireless electronic measurement system and stability of wireless operation utilizing BWIMP sensing platform. (A) Schematic illustration of the customized system consisting of a surgery table where an animal subject can lie, a freely movable primary antenna that wirelessly delivers power to and communicates data from the loop antenna built in the sensing device, a reader, and a PC for real-time monitoring of the sensor signals. (B) Schematic diagram of an electrical circuit corresponding to the overall system. (C) Magnetic field distribution for the single primary antenna. (D) Maximum distance between the primary antenna and sensing device, which is capable of wireless data communication, according to position in the X-Y plane. (E, F) Responses of a wireless temperature sensor and wireless T-C strain sensor (i) under sequential approach of tweezers to the sensing device and (ii) under repetitive lateral movement of the sensing device by 5 cm, respectively, with associated photographs.

2.4. Performance of the battery-free, wireless sensing system and in vitro real-time monitoring

Figure 4A-C highlight the wireless temperature and strain sensing performances of the BWIMP sensing platform. Figure 4A compares the responses of the wireless temperature sensor to temperature and strain stimuli. The results show that the wireless temperature sensing feature maintains reasonable sensitivity (6.2mV/°C), high linearity (R^2=0.99), and negligible hysteresis (0.29%) under heating and cooling and it is insensitive to the external strain, even under wireless measurement conditions. Figure 4B presents the responses of the wireless T-C strain sensor to temperature and strain stimuli, indicating decoupled strain sensing features with reasonable sensitivity (1.9mV/%), high linearity (R^2=0.99), minimum hysteresis (3.6%), and insensitivity to external temperature change. In addition, Figure 4C reveals mechanical/electrical durability and high repeatability under 500 repeated cycles of 10% strain (ΔV_{out} of 20 mV remains constant) (under 5,000 repeted cycles in Figure S17). These results support the capability of independent detection of each physical parameter (temperature and strain) from the multimodal sensors in the wireless measurement system.

Figure 4D-I summarize the feasibility of wireless, continuous monitoring of temperature and strain in an *in vitro* experiment mimicking the *in vivo* environment (nerve or blood vessel system). Figure 4D presents a schematic illustration of the *in vitro* testing setup, which consists of a syringe pump (NE1010, New Era, US) with a surrounding heater, a deformable elastomer tube (Dragon Skin 30, Smooth-On), a valve, and the abovementioned wireless measurement electronic system (Figure 3A). As illustrated in Figure 4E, this setup facilitates simultaneous control of the temperature and strain inputs applied to the sensors conformally wrapped around the elastomer tube: (i) temperature change by the heated deionized (DI) water source and (ii) strain change by increasing/decreasing the diameter of the elastomer tube via valve opening/closing control. Figure 4F shows a photograph of the thin, cuff-type sensor encircling the elastomer tube (outer diameter = 4 mm; inner diameter = 3.5 mm). The magnified images in Figure 4G clearly present the conformal contact of the sensors with the elastomer tube before and after expansion (ε = 0% and 10%, respectively). Figure 4H and I show the *in vitro* monitoring results, presenting the signals of the wireless temperature and T-C strain sensors, and the measured temperature and strain values at the same timeline under different conditions. In Figure 4H (i), the wireless T-C strain sensor exhibits instant responses to sequential loading and unloading of strains (ε = 10%), whereas the wireless temperature sensor is insensitive to the applied strain changes. On the other hand, as shown in Figure 4H (ii), the signals collected from the wireless temperature sensor clearly undergo a temperature change of 2.5 °C after

heating, whereas those obtained using the wireless T-C strain sensor remain constant. These results indicate that each sensor is capable of real-time decoupling of temperature and strain stimuli. *In vivo* clinical trials can involve very slow changes in the physical state of the nerves. In humans, the length of axonal regeneration is known to be 1-2 mm/day typically [46]. To mimic the long-term situation, a gradual strain was applied for 8 h without an artificial temperature change. Figure 4I shows that the wireless sensing platform can monitor the gradual change in strain of 4% and natural change in ambient temperature of 0.7 °C, without instability of the wireless operation and data read-out of this system. These results demonstrate the feasibility and stability of wireless, continuous, long-term, and independent temperature and strain monitoring using the BWIMP sensing platform, which supports the ability to perform the continuous nerve monitoring.

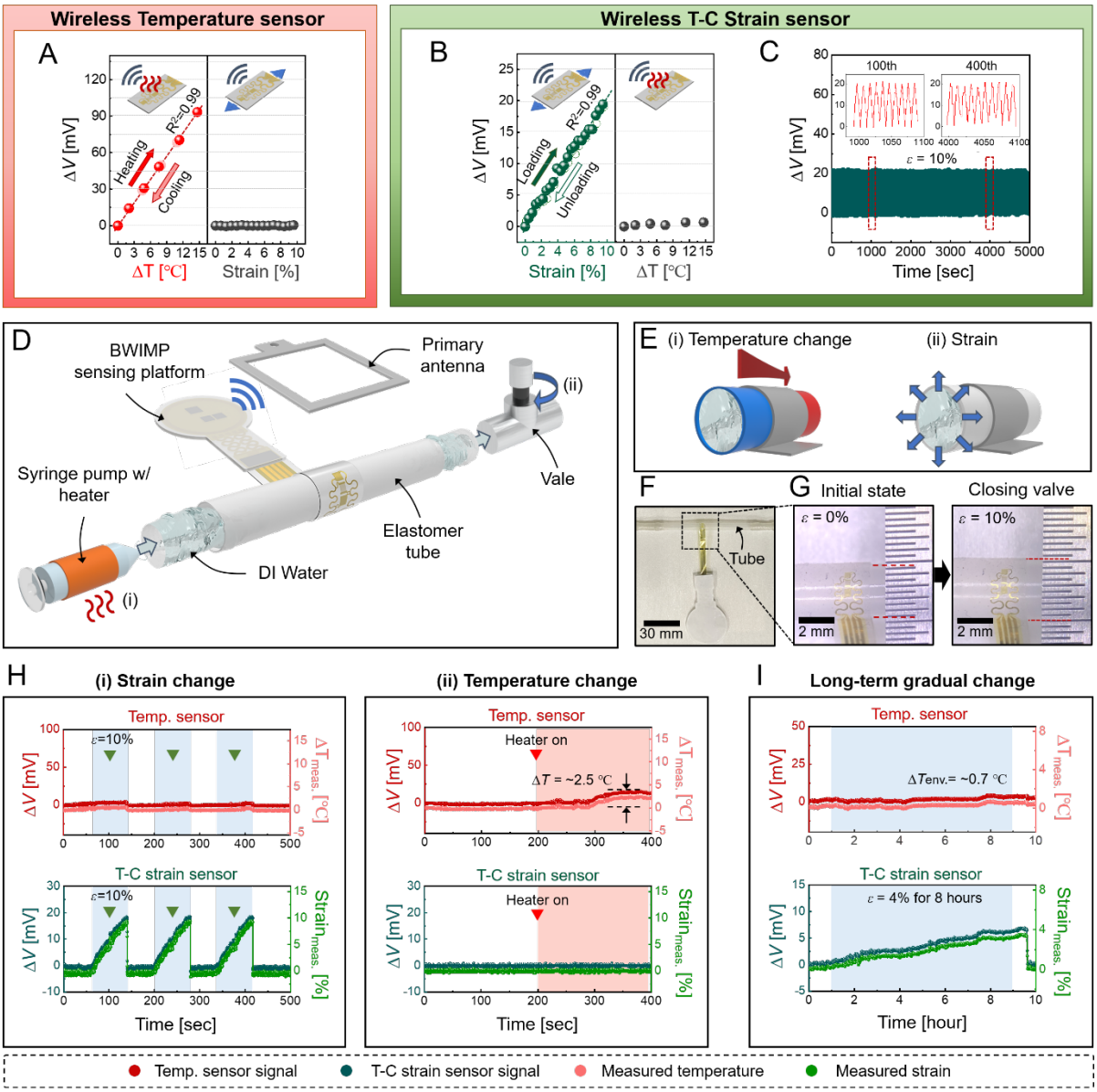

Figure 4. Performance characterization of the BWIMP sensing platform and demonstration of wireless *in vitro* monitoring in an artificial nerve model. (A) Temperature- and strain-response curves of a wireless temperature sensor (under ΔT of 0-15 ℃ and ε of 0-10%). (B) Strain- and temperature-response curves of a wireless T-C strain sensor (under ΔT of 0-15 ℃ and ε of 0-10%). (C) Cyclic responses of the wireless T-C strain sensor under 500 repetitive loading-unloading cycles with an applied strain of 10%. The insets present the signals at the 100th and 400th cycles. (D) Schematic illustration of an *in vitro* testing set-up composed of a soft elastomer tube (Dragon skin 30), a syringe pump covered by a heater at the inlet, and a valve at the outlet. (E) Schematic illustration of controllable stimuli exerted to the sensing device. (i) change in temperature caused by heated DI water source; (ii) strain input induced by the diameter change via the valve control. (F) Photograph of the sensing device mounted on the elastomer tube. (G) Comparative microscopic images of before and after expansion of the elastomer tube (strain 10%). (H) Responses of the wireless temperature and the wireless T-C strain sensors, and curves of measured temperature change and strain, during (i) sequential strain inputs of 10% and (ii) a temperature change of 2.5 ℃, respectively. (I) Long-term responses under prolonged, gradual strain input of 4% for 8 h and natural ambient temperature change.

2.5. Evaluation of feasibility and stability of *in vivo* operation

Capabilities for continuous *in vivo* nerve monitoring rely on a wrapping method that supports conformal contact of the sensing device for high accuracy of collected data, even in moist or wet environments that typically arise from bleeding and/or fluid from scars. Here, the proposed wrapping method using a medical endo-clip leads to the tightening of two electrode layers of the BWIMP sensing platform in contact with each other after the cuff-type sensors encircle a target nerve without any chemical treatment. Figure 5A (i) shows a schematic illustration of a wrapping method without the endo-clip, which can lead to delamination of the two layers owing to weakening of the adhesion forces due to the penetration of the biofluids into the interfacial gap. The device may peel off the nerve, generating abnormal signals. On the other hand, Figure 5A (ii) presents a schematic illustration of the wrapping method with the endo-clipping for tightening both two electrode layers. The covered PI layers (thickness of 50 μm for each layer) protect the two stacked electrode layers from physical damage on both sides by squeezing the endo clip. This approach provides minimum movement of the contact interface between the wireless sensor and target nerve and maintains a good conformal contact, resulting in stable and accurate nerve monitoring . Figure 5A (iii) shows a photograph of the BWIMP sensing platform wrapped around the sciatic nerve of an animal subject (rat) and fixed with an endo-clip. Movie

S1 clearly shows the stable sensing device despite artificial external stimuli that try to move the sensor.

Figure 5B presents a schematic illustration of the *in vivo* animal testing setup (using the abovementioned wireless measurement system in Figure 3A) for evaluating the feasibility and stability of the operation for practical *in vivo* nerve monitoring. This approach provides the real-time visualization of signals collected from the implanted sensing device wrapped around the sciatic nerve of an animal. Figure 5C and S18 show the *in vivo* testing results for a small animal (a rat, body weight 150 g-200 g) and a medium animal (a rabbit, body weight 2-2.5 kg), respectively. Both results exhibit no significant instability of the voltage signals (ΔV) within 5 min after wrapping the sensors around the nerves, except for a slight gradual increase of 0.2-0.3°C arising from temperature equilibrium with the target sciatic nerves. These approaches for clinical trials on small and medium animals, which have much smaller peripheral nerves than humans (large animals), provide the possibility for use in continuous *in vivo* monitoring in humans. In addition, Figure S19 provides photographs of a completely subcutaneously implanted wireless device, even inside a small animal (rat).

Figure 5D and E summarize the stability of the voltage signals under *in vivo* electrical and mechanical stimuli, respectively. Figure 5D shows that the responses are insensitive to the electrical stimulation applied to the proximal site of the target sciatic nerve. The inset shows a schematic illustration of the electrical stimulation through wired electrodes, including sequential electrical pulses (five repetition of an action potential of 100 mV and a resting potential of 0 mV). Figure 5E also exhibits no noticeable fluctuations in the voltage signals measured from the wireless device regardless of the external physical stimulation. The inset shows a schematic illustration of physical stimulation that includes a gentle touch of the leg of the subject animal in which the wireless sensor is implanted. These results indicate the possibility of incorporating nerve monitoring via the BWIMP sensing platform with various electrical or mechanical stimulations for the acceleration of neuro-regeneration and functional recovery.

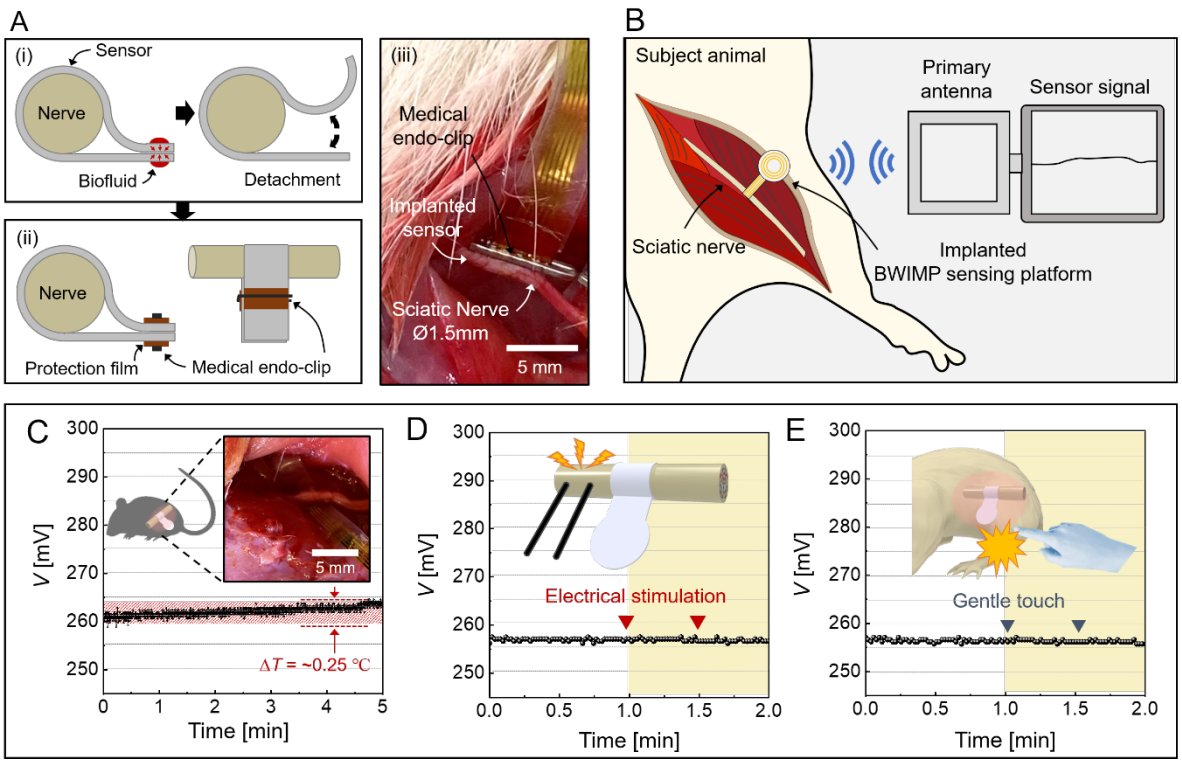

Figure 5. Stability of wireless *in vivo* operation of BWIMP sensing platform at surgical implantation. (A) (i) Schematic illustration of a delamination issue due to a wet environment caused by surrounding biofluids (*e.g.*, bleeding and/or fluid from a scar), (ii) a proposed medical endo-clipping technique for improvement of conformal contact and minimum movement of the sensing device, (iii) photograph of a sensing device implanted on a sciatic nerve of a subject animal fixed by the endo-clip. (B) Schematic illustration of an *in vivo* setup presenting a BWIMP sensing device wrapped around a sciatic nerve of a subject animal and wireless sensor signal communication. (C) Photographs of implantation of the sensing device on a sciatic nerve of a rat and wireless sensor signals at a certain period (*e.g.*, 5 min after mounting). (D, E) Wireless sensor signals under sequential electrical and physical stimuli (*i.e.*, gentle touching of the leg of the subject animal with a hand), respectively.

2.6. Battery-free, wireless, continuous *in vivo* nerve monitoring

Figure 6A presents a schematic illustration of an *in vivo* animal test (rats) for evaluating the ability of the BWIMP sensing platform to perform continuous postoperative nerve monitoring. The two BWIMP sensing platforms transfer data collected from each sensor wrapped around the two sciatic nerves locations (proximal and distal sites) to the NFC reader and primary antenna for real-time nerve monitoring. Figure 6B and S20 show schematic illustrations of continuous measurement processes at the proximal and distal sites of (i) a normal nerve and (ii)

a crushed injured nerve induced by acute traumatic compression for immediate clinical change. Figure 6C provides photographs of the surgical procedures: (i) incision of the thigh skin to expose the sciatic nerve with a diameter of 1.5-2 mm; (ii) implantation of two devices around the normal nerve at both proximal and distal sites where the medical endo-clips hold the electrode regions to minimize the spacing between the sensor and the nerve; (iii) generation of a crushed nerve injury by acute traumatic compression (inset); and (iv) closing of the surgery site. Figure S21 presents photographs of the crushed sciatic nerve formed by compression using forceps for 15 s. Such acute short-term compression is a common case of peripheral nerve injury, resulting in nerve ischemia, hypoxia, edema, increased vascular permeability, and blocking of axoplasmic flow [47]. After the peripheral nerve injury, the nerve microcirculation plays an important role in regulating the nerve microenvironment and neurotrophic substances, supplying blood and oxygen, and maintaining neural conduction and axonal transport.

Figure 6D and E depict the responses to changes in temperature and strain obtained from each wireless device wrapped around a crushed nerve at both proximal and distal sites for 80 min. The continuous *in vivo* monitoring of physiological signals in the early stage can provide quantitative information regarding the damage level of nerves and instant corresponding treatment. In Figure 6D (i) and E (i), the data collected from both the proximal and distal sites exhibit temperature increases of 0.3 °C and 0.6 °C, respectively. Figure S22 depicts the reproducibility of these trends measured by wired sensors for three individual animals (N = 3, rats). After the crushed injury by nerve compression, an inflammatory reaction, which usually accompany with the temperature raise at the injury, increases the local vascular permeability and generates subsequent intraneural edema. The occurrence of edema greatly alters the microenvironment of the nerve by increasing the local pressure, thereby decreasing the blood flow. Therefore, the BWIMP sensing platform capable of detecting physical changes based on the inflammatory reaction could enable early warning and diagnosis in various clinical scenarios, including situations involving unexpected complications due to multiple and severe nerve damage. The data in Figure 6D (ii) and E (ii), collected from both the proximal and distal sites, exhibit a strain increases of 3.0% and 2.0% due to combination of local strain by bottleneck microcirculation and squeezing of the nerve stump by compression. These results support that the ability to perform quantitative and continuous strain measurements can identify clinical scenarios for the postoperative nerves (*e.g.* nerve expansion or shrinkage caused by abnormal/normal nerve regeneration, *etc*.).

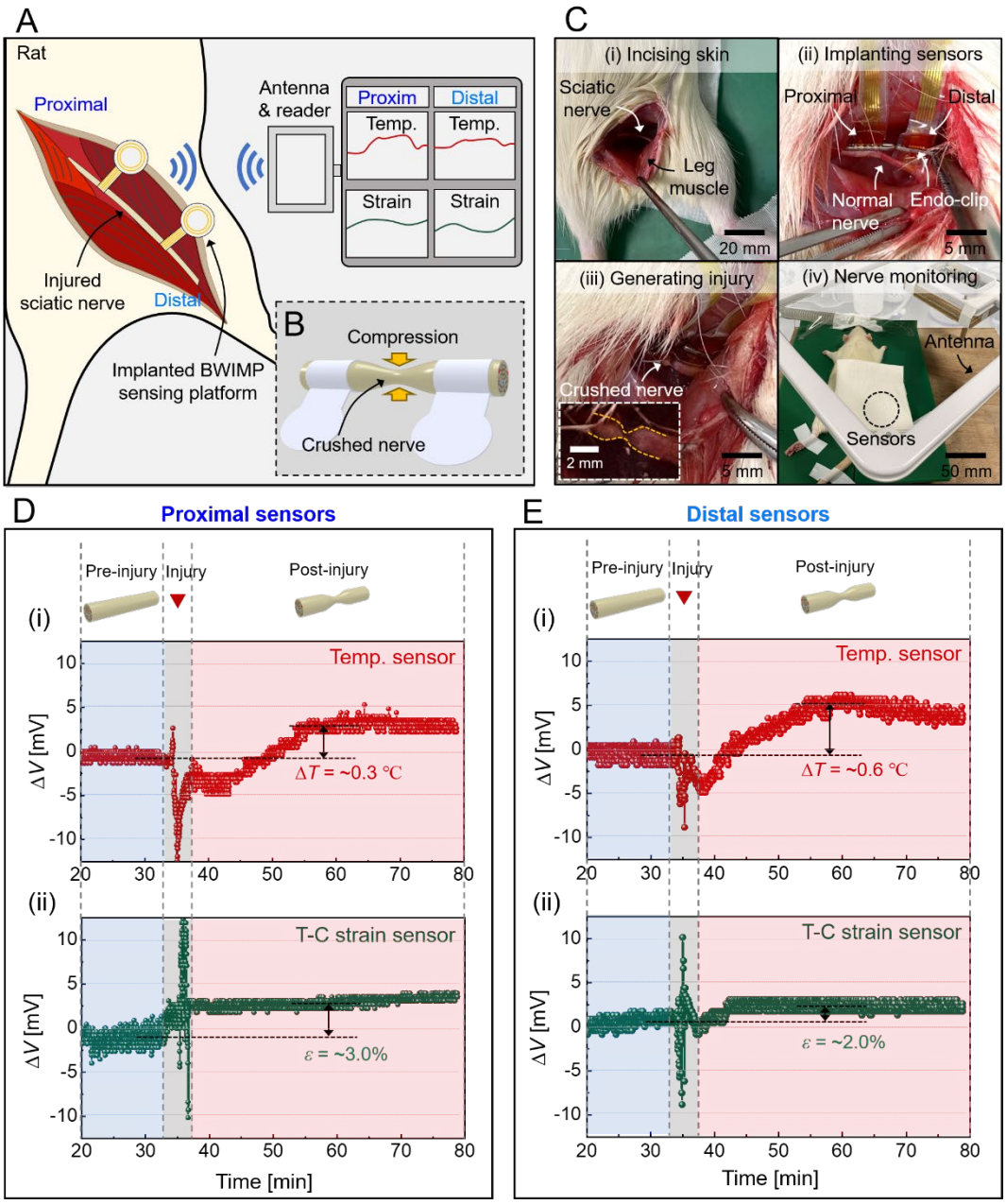

Figure 6. Demonstration of wireless nerve monitoring of the sciatic nerve in a rodent model (rats) utilizing the BWIMP sensing platform. (A) Schematic illustration of an *in vivo* testing setup. Two BWIMP sensing devices wrapped around the sciatic nerves of a rat detect the changes in the physical states (temperature and strain) and wirelessly transfer the detected information to the primary antenna for real-time, visible monitoring. (B) Schematic illustration of the crushed nerve injury by acute traumatic compression. (C) Photographs of surgical procedures. (i) Thigh skin is incised to expose the sciatic nerve with a diameter of 1.5~2 mm; (ii) two sensing devices are implanted (normal nerve) where the medical endo-clips hold the electrode regions; (iii) crushed nerve injury is generated; (iv) the implantation site is closed. (D, E) Continuous responses collected from wireless devices wrapped around both the proximal

and distal sites for 80 min, respectively, with quantitatively measured values of the changes in temperature and strain due to the nerve injury.

2.7 Biocompatibility of BWIMP sensing platform

The biocompatibility of the electrode of the BWIMP sensing platform is a critical factor for its application in long-term *in- vivo* monitoring of nerve regeneration states. We demonstrate the biocompatibility of individual materials used in devices, a necessary step for clinical trials. The biocompatibility test using mice was performed with reference to previous results in which mice responded more sensitively than rats in implantation toxicity tests.[48] The prepared electrode samples (5 mm × 10 mm; changeable) composed of multi-layered Ecoflex/PI/Au/PI/Ecoflex (100 μm thickness) were subcutaneously inserted into individual Balb/c mice and yielded data on foreign body reactions. The results in Figure S23A indicate that the changes in weight of mice with electrode implants, as controls, and those with inert polydimethylsiloxane (PDMS) film (100 μm thickness) implants were similar throughout the four weeks of observation. Following implantation, the mice behaved normally with no substantial skin necrosis or swelling for up to four weeks. Hematoxylin and eosin (H&E) stained sections of implant sites surrounding tissues and major organs (the heart, kidney, liver, lung, and spleen) showed comparable levels of immune cell infiltration and systemic toxicity between PDMS- and Ecoflex-implanted tissues on day 28 (Figure 7A). Some minimal inflammatory responses and fibrosis appear close to the implants, but no significant evidence of injury or cell death occurs in the adjacent tissue. Histological studies provided further support for the biocompatibility of the material, as shown in Figure 7B. The four spot images (histologically analyzed area 0.16 mm^2) selected randomly from each organ showed no significant differences between the reference (PDMS) and test (Ecoflex) groups. In addition, Figure S23B and C show immune cell counts from the adjacent skin in representative H&E staining images, providing additional evidence of the biocompatibility of Ecoflex. Fibrosis scores on Masson trichrome staining were as follows: none = 0, mild = 1, moderate = 2, and severe = 3. As shown in Figure 7C, S23D, and S23E, the result shows that the fibrosis score for Ecoflex is almost the same as that of PDMS, which additionally supports the *in vivo* biocompatibility of the sensor.

The results of complete blood count provide a comprehensive understanding of the health of mice. The white blood cell, neutrophil, lymphocyte, and monocyte counts are not significantly different between the reference and test groups, indicating that bacterial infection, viral infection, and critical immune responses did not occur during implantation (Figure 7D-G). In

addition, the similarity of the red blood cell and platelet counts between the groups suggests that no toxicity or damage occurred in the implanted device. (Figure S23F-I).

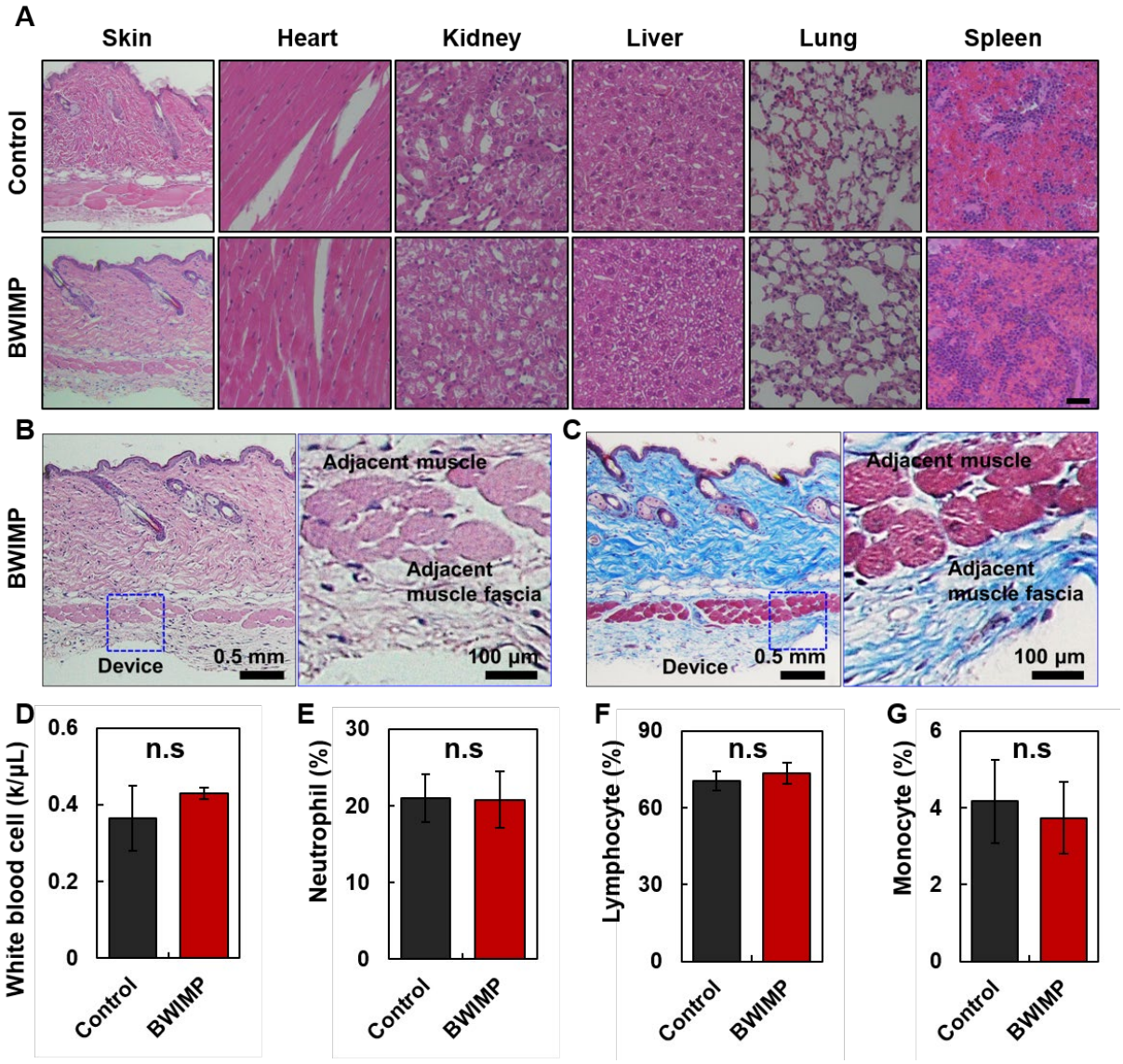

Figure 7. *In vivo* biocompatibility of constituent materials of BWIMP sensing platform. (A) Hematoxylin and eosin (H&E) stained sections obtained in skin and major organs (heart, kidney, liver, lung, and spleen) 4-week post implantation of PDMS (control group) and Ecoflex (test group). The scale bar presents 200 µm. (B) H&E staining images and (C) Masson trichrome staining images were obtained after 4 weeks of Ecoflex implantation. In (B) and (C), the right-hand images show magnified versions of the adjacent muscle fascia and muscle tissue. The complete count results of (D) White blood cell, (E) Neutrophil, (F) Lymphocyte, and (G) Monocyte for reference controls and test groups (n=3 per groups), showing no significant differences between the groups.

3. Conclusion

This study introduces a battery-free, wireless, fully implantable, multimodal physical sensing platform that supports continuous *in vivo* monitoring of temperature and strain *via* thin, soft, and cuff-type sensors wrapped around the nerve. The wireless device exhibits reasonable sensitivity, excellent stability, high linearity, and minimum hysteresis in the relevant ranges. The data collected by multiple devices interfaced at the proximal and distal sites provide an accurate, quantitative basis for change in temperature and volume of nerve after surgery. In particular, the strain sensors integrated with temperature-compensated circuits enable accurate strain measurement with negligible temperature dependence. In addition, the system supports a long-range (13 cm) power harvesting and data communication to fully implanted devices wrapped around the nerves of subject animals regardless of their size. Experimental evaluations, verified by numerical simulations, as well as clinical trials on subject animals, demonstrate the feasibility and stability of the sensor system for continuous nerve monitoring.

The additional sensors capable of measuring hemodynamics integrated with the battery-free, wireless sensing platforms could enhance our understanding of the mechanism for functional recovery of injured nerve. Capabilities for continuous, long-term *in vivo* monitoring (a few weeks or months) of various physiological signals at multiple sites could support not only accurate diagnosis and evaluation of nerve regeneration, but also neuropathic pain treatment using local cooling. In addition, the component replacement of the sensor and wireless platform with bioresorbable materials can provide advanced functionality without secondary surgical removal process for practical use in a variety of implantable applications. Finally, animal tests conducted on numerous animals using the battery-free, wireless sensor system reported herein could support quantitative basis for defining algorithms or thresholds of functional recovery of injured nerve depending on therapies for improving regeneration along with wireless electrical, optogenetic, and pharmacologic stimuli.

4. Experimental Section/Methods

Fabrication of the cuff-type, implantable, multimodal physical sensor: Fabrication began with the formation of a PI film (thickness 2.5 μm, PI-1338, VTEC^{TM}) on a Si wafer via spin coating (5000-7000 rpm for 30 s) and curing (250 ℃ for 4 h) of PI solution. The first photolithography step defined a photoresist pattern (AZ 5214E, Micro Chem, spin-coating at 5000 rpm; soft-bake at 110 ℃ for 1 min; exposure for 8 sec; development in AZ 300 MIF for 1min), enabling the patterning of a Ti/Au membrane (thickness 20 nm/50 nm) deposited on the top of the PI film using electron beam (E-beam) evaporation through a lift-off process, and forming conductive

active layers of sensors, interconnects, and electrodes. The second sequential photolithography, E-beam evaporation, and lift-off process yielded a Ni membrane (thickness 100 nm) at the end of the electrode, which acted as a mask for reactive ion etching (RIE). Subsequently, additional spin coating (5000-7000 rpm for 30 s) and curing (250 ℃ for 4h) of the PI film completely encapsulated the patterned Ti/Au membrane. The resulting thickness of the PI/Au/PI was 5 μm. The third photolithography, e-beam evaporation, and lift-off process deposited a Ni membrane pattern corresponding to the designed outlines of the sensors, interconnects, and electrodes on top of the PI film, as an RIE mask. Etching of the PI film via RIE (STEALTHYON 800, SORONA, O_2, 150 W, 40 sccm, 30 min) except in the region protected by the Ni membrane and removal of the Ni membrane using an etchant (TFB, Transene) completed a patterned PI/Au/PI film with open contact pads at the end of the electrode. Next, polyvinyl alcohol (PVA)-based water-soluble tape (5425, 3M) was used to transfer the patterned PI/Au/PI film to a spin-coated (1500 rpm for 30 s) and partially cured elastomer matrix (thickness 50 μm, Ecoflex 0030, Smooth-On, Inc.). After dissolving the water-soluble tape in hot water (65 ℃), additionally spin coated (1500 rpm for 30 s) and cured (70 ℃ for 2 h) elastomer matrix (thickness 50 μm) covered the tri-layered film (PI/Au/PI), except for the open contact pads by blocking the area with an elastomer film before spin coating. The total thickness of the Ecoflex/PI/Au/PI/Ecoflex stack was 100 μm. Cutting the free-standing structure into a desired shape and dimensions using blades yielded a cuff-type sensor (width 4 mm; length 35 mm; thickness 100 μm).

Manufacturing of NFC SoC: The process began with the patterning of electrical circuits (Au membrane thickness 10 μm) on an FPCB substrate (thickness 150 μm, Pyralux AP8535R, DuPont) for the formation of a spiral loop antenna, bonding with electronic components, and connection to the cuff-type sensor. Subsequently, the outline of the FPCB substrate was cut using a laser ablation machine (ProtoLaser U4, LPKF). The electronic components, including an NFC chip (RF430FRL154H, Texas Instruments), two amplifiers (INA333, Texas Instruments), resistors, capacitors, and an FFC connector, were soldered onto the open pads in the FPCB substrate. The printed spiral loop antenna has a diameter of 20 mm with five turns, and a tuning capacitor (GJM03-KIAT-TTOL-DE, Murata Electronics) regulated the natural frequency of the NFC SoC to 13.56 MHz. The 5-mm-pitch FFC connector was designed to accurately align its connector pins and the electrodes of the cuff-type sensor, enabling the temperature/strain sensors to connect with the Wheatstone bridge circuits.

Characterization of the temperature and strain sensors: The experimental setup for the evaluation of temperature sensor included a customized convection chamber to apply controlled heat and thermocouples for feedback control of the temperature (resolution = approximately 1 ℃). The experimental setup for the evaluation of the strain sensor included a linear stage machine to apply strain with controlled loading and unloading rates and a stretchable elastomer substrate (Ecoflex 0030, thickness 1 mm) where the sensor could be attached. A digital multimeter (NI-USB 4065 Digital Multimeter, National Instruments) was used to measure the resistances and output voltages of both wired sensors. In case of the wireless sensing platform, the abovementioned setup was placed on the surgery table with the primary antenna and NFC reader, which received the ADC signals from the NFC SoC.

NFC protocols and software operation: A wireless reader (TRF7970AEVM, Texas Instruments) provided the writing process in the NFC SoC using a custom graphical user interface in the ISO 15693 protocol. The NFC reader enabled data communication and wireless energy harvesting via an antenna reader (ID ISC. LRM2500-A, FEIG) with a transmission antenna. ISOStart 2018 software supported continuous, real-time data acquisition of ADC values from the NFC SoC. Developed software based on Python provided the classification and visualization of the collected data. Since NFC chips have unique product numbers (e.g. D39B, E8AC, etc.), data from multiple devices can be differentiated.

Finite element analysis (FEA) for mechanical and electromagnetic simulation: The commercial software ANSYS Mechanics (Ansys, USA) was used to simulate the strain distribution generated on the BWIMP sensing platform under mechanical stimuli. The mechanical simulation results confirmed the mechanical reliability and stability by checking (i) no failure ($\varepsilon < \varepsilon_{fracture}$) in the components of the cuff-type, multimodal physical sensor, including the Au membrane (thickness = 50 nm), PI film (thickness = 5 μm), and elastomer matrix (thickness = 100 μm) under stretching conditions. The mechanical properties [elastic modulus (E) and Poisson's ratio (υ)] of the constituting materials were E_{Au} = 79 GPa / υ_{Au} = 0.42 for the Au membrane, E_{PI} = 3.2 GPa / υ_{PI} = 0.34 for the PI film, and $E_{Ecoflex0030}$ = 69.8kPa / $\upsilon_{Ecoflex0030}$ = 0.49 for the elastomer matrix. The commercial software ANSYS HFSS (ANSYS, USA) was used to simulate the electromagnetic field distribution created around the primary antenna operating at 13.56 MHz. The magnetic simulation results derived an operating range capable of wireless data communication *via* the strength and direction of the computed magnetic field distribution.

In vitro characterization of the temperature and strain sensing: The *in vitro* experimental setup for the evaluation of real-time and simultaneous temperature and strain sensing contained a syringe pump (NE1010, New Era, USA), a rubber heating pad surrounding the syringe with a heater controller (New Era Pump Systems Syringe Heater Kit, New Era, USA), a customized elastomer tube (Dragon Skin 30; diameter 4 mm; shell thickness = 0.5 mm), a valve, commercial silicon tubes (hswmall, diameter = 4 mm; shell thickness = 0.5 mm) connecting to these devices, and two thermocouples inserted inside the tubes (Super OMEGACLADTM XL, Omega, inc., USA). This setup was combined with the abovementioned primary antenna for NFC-based wireless sensing. The heater operated while injecting the source water into the elastomer tube with the syringe pump, and the temperature of the injected water increased gradually; thus, the sensor attached to the elastomer tube received heat *via* conduction. The valve was closed while injecting the source water into the elastomer tube with the syringe pump, and the water was trapped inside the passage; eventually, only the softest elastomer expanded, and strain was applied to the sensor.

Implantation of BWIMP sensing platform and continuous nerve monitoring: The implantation of the BWIMP sensing platform began with incision of the thigh of a rat or a rabbit model. The sciatic nerve was observed when the incised muscles were spread. The diameter of the sciatic nerve of the rat was 1.5-2 mm and that of the rabbit was 2-2.5 mm. The wireless devices were wrapped around the normal sciatic nerve. The incision area was covered with the muscles to prevent input of external air. The wireless measurement system recorded the signals of the sensors. For electrical stimulation, wired Pt electrodes were inserted to the nerve and electrical pulses (five repetition of an action potential of 100 mV and a resting potential of 0 mV) were applied with a function generator (AFG1062, Tecktronix, USA). For generation of crushed nerve injury, the covered muscles were opened again using forceps and a consistent compression was applied to the nerve with forceps for 15s after the temperature reached a steady state. After covering the incision area again, the sensor signals of both the proximal and distal sensors were continuously measured.

Assessment of biocompatibility: All procedures were approved by the Institutional Animal Care and Use Committee of the Korea Institute of Science and Technology (IRB. No. KIST-2021-079) and Korea University (IRB. No. KOREA-2020-0149). Male Balb/c (6-week-old) mice were purchased from Narabio, Korea. The mice were anesthetized with isoflurane gas (2%), and autoclave sterilized samples of PDMS (5 mm × 10 mm), PI (5 mm × 10 mm), and Ecoflex

(5 mm × 10 mm) were implanted subcutaneously through dorsal incision. After implantation, the wound was stitched with 6-0 black silk (Alee Co., Korea) and dressed with a Tegaderm film (3M Science, USA). Daily checking, weighing, and care of the mice ensured moribund conditions and regular stress exposure. The mice were sacrificed for histological analysis at 28 days after implantation. The skin was sliced and fixed in 4% paraformaldehyde solution, embedded in paraffin, sectioned, and stained with H&E, Masson trichrome for histological analysis. Whole blood samples were collected in ethylenediaminetetraacetic acid (EDTA)-treated tubes to evaluate the complete blood count (Neodin BioVet, Korea). The major organs (heart, kidney, liver, lung, and spleen) were extracted to assess systemic toxicity. Histological scores were assessed as previously described. [49]

Supporting Information

Supporting Information is available from the Wiley Online Library or from the author.

Acknowledgements

S.K and I.P were supported by the National Research Foundation of Korea (NRF) grant funded by the Korea Government (MSIT) (2021R1A2C3008742). Y.S.O was supported by Basic Science Research Program through the National Research Foundation of Korea (NRF) funded by the Ministry of Education (2020R1I1A1A0107489711). Z.X. acknowledges the support from the National Natural Science Foundation of China (Grant No. 12072057) J.K. was supported by the National Research Foundation of Korea (NRF) grant funded by the Korea Government (MSIT) (2021R1A2C2094799).

Conflict of Interest

All authors declare that they have no competing interests.

Data Availability Statement

Additional data related to this paper may be requested from
the corresponding authors upon reasonable request.

Received: ((will be filled in by the editorial staff))
Revised: ((will be filled in by the editorial staff))
Published online: ((will be filled in by the editorial staff))

[1] C. A. Taylor, D. Braza, J. B. Rice, T. Dillingham, *Am. J. Phys. Med. Rehabil.* **2008**, *87*, 381.

[2] D. Grinsell, C. P. Keating, *Biomed Res. Int.* **2014**, *2014*, 698256.

[3] S. W. P. Kemp, P. S. Cederna, R. Midha, *Exp. Neurol.* **2017**, *287*, 348.

[4] G. Lundborg, *J. Peripher. Nerv. Syst.* **2003**, *8*, 209.

[5] S. K. Lee, S. W. Wolfe, *J. Am. Acad. Orthop. Surg.* **2000**, *8*, 243.

[6] J. Noble, C. A. Munro, V. S. S. V Prasad, R. Midha, *J. Trauma Acute Care Surg.* **1998**, *45*.

[7] D. R. Smith, A. I. Kobrine, H. V Rizzoli, *J. Neurol. Sci.* **1977**, *33*, 341.

[8] K. AUKLAND, B. F. BOWER, R. W. BERLINER, *Circ. Res.* **1964**, *14*, 164.

[9] D. W. Zochodne, L. T. Ho, *Brain Res.* **1990**, *535*, 43.

[10] P. A. Low, R. R. Tuck, *J. Physiol.* **1984**, *347*, 513.

[11] B. Rydevik, G. Lundborg, U. Bagge, *J. Hand Surg. Am.* **1981**, *6*, 3.

[12] I. M. Jou, K. A. Lai, C. L. Shen, Y. Yamano, *J. Orthop. Res. Off. Publ. Orthop. Res. Soc.* **2000**, *18*, 149.

[13] D. G. Kline, E. R. Hackett, G. D. Davis, M. B. Myers, *J. Surg. Res.* **1972**, *12*, 254.

[14] D. N. e Silva, J. Coelho, F. de O. Frazílio, A. N. Odashiro, P. de T. C. de Carvalho, E. R. J. C. Pontes, A. F. Vargas, M. Rosseto, A. B. A. da Silva, *Acta Cir. Bras.* **2010**, *25*, 158.

[15] H. Teymur, Y. O. Tiftikcioglu, T. Cavusoglu, B. I. Tiftikcioglu, O. Erbas, G. Yigitturk, Y. Uyanikgil, *Kaohsiung J. Med. Sci.* **2017**, *33*, 69.

[16] A.-L. Cattin, J. J. Burden, L. Van Emmenis, F. E. Mackenzie, J. J. A. Hoving, N. Garcia Calavia, Y. Guo, M. McLaughlin, L. H. Rosenberg, V. Quereda, D. Jamecna, I. Napoli, S. Parrinello, T. Enver, C. Ruhrberg, A. C. Lloyd, *Cell* **2015**, *162*, 1127.

[17] Y.-G. Zhang, Q.-S. Sheng, H.-K. Wang, L. Lv, J. Zhang, J.-M. Chen, H. Xu, *Neurosci. Lett.* **2014**, *561*, 198.

[18] R. B. Stein, D. Charles, T. Gordon, J.-A. Hoffer, J. Jhamandas, *IEEE Trans. Biomed. Eng.* **1978**, *BME-25*, 532.

[19] A. Fouchard, V. Coizet, V. Sinniger, D. Clarençon, K. Pernet-Gallay, S. Bonnet, O. David, *J. Physiol.* **2016**, *110*, 361.

[20] S. S. Burks, D. J. Levi, S. Hayes, A. D. Levi, *J. Neurosurg.* **2014**, *121*, 210.

[21] C. Yi, L. B. Dahlin, *Neuroreport* **2010**, *21*, 958.

[22] M. D. Wood, S. W. P. Kemp, C. Weber, G. H. Borschel, T. Gordon, *Ann. Anat. - Anat. Anzeiger* **2011**, *193*, 321.

[23] X. Zhang, W. Qu, D. Li, K. Shi, R. Li, Y. Han, E. Jin, J. Ding, X. Chen, *Adv. Mater. Interfaces* **2020**, *7*, 2000225.

[24] R. Li, Z. Liu, Y. Pan, L. Chen, Z. Zhang, L. Lu, *Cell Biochem. Biophys.* **2014**, *68*, 449.

[25] C. M. Boutry, L. Beker, Y. Kaizawa, C. Vassos, H. Tran, A. C. Hinckley, R. Pfattner, S. Niu, J. Li, J. Claverie, Z. Wang, J. Chang, P. M. Fox, Z. Bao, *Nat. Biomed. Eng.* **2019**, *3*, 47.

[26] C. M. Boutry, Y. Kaizawa, B. C. Schroeder, A. Chortos, A. Legrand, Z. Wang, J. Chang, P. Fox, Z. Bao, *Nat. Electron.* **2018**, *1*, 314.

[27] J. T. Reeder, Z. Xie, Q. Yang, M.-H. Seo, Y. Yan, Y. Deng, K. R. Jinkins, S. R. Krishnan, C. Liu, S. McKay, E. Patnaude, A. Johnson, Z. Zhao, M. J. Kim, Y. Xu, I. Huang, R. Avila, C. Felicelli, E. Ray, X. Guo, W. Z. Ray, Y. Huang, M. R. MacEwan, J. A. Rogers, *Science (80-.).* **2022**, *377*, 109.

[28] S.-K. Kang, R. K. J. Murphy, S.-W. Hwang, S. M. Lee, D. V Harburg, N. A. Krueger, J. Shin, P. Gamble, H. Cheng, S. Yu, Z. Liu, J. G. McCall, M. Stephen, H. Ying, J. Kim, G. Park, R. C. Webb, C. H. Lee, S. Chung, D. S. Wie, A. D. Gujar, B. Vemulapalli, A. H. Kim, K.-M. Lee, J. Cheng, Y. Huang, S. H. Lee, P. V Braun, W. Z. Ray, J. A. Rogers, *Nature* **2016**, *530*, 71.

[29] J. Ausra, S. J. Munger, A. Azami, A. Burton, R. Peralta, J. E. Miller, P. Gutruf, *Nat. Commun.* **2021**, *12*, 1968.

[30] G. Gagnon-Turcotte, Y. Lechasseur, C. Bories, Y. Messaddeq, Y. De Koninck, B. Gosselin, *IEEE Trans. Biomed. Circuits Syst.* **2017**, *11*, 1.

[31] M. Hashimoto, A. Hata, T. Miyata, H. Hirase, *Neurophotonics* **2014**, *1*, 1.

[32] T. Stuart, W. J. Jeang, R. A. Slivicki, B. J. Brown, A. Burton, V. E. Brings, L. C. Alarcón-Segovia, P. Agyare, S. Ruiz, A. Tyree, L. Pruitt, S. Madhvapathy, M. Niemiec, J. Zhuang, S. Krishnan, B. A. Copits, J. A. Rogers, R. W. I. V Gereau, V. K. Samineni, A. J. Bandodkar, P. Gutruf, *ACS Nano* **2023**, *17*, 561.

[33] Y. Zhang, A. D. Mickle, P. Gutruf, L. A. McIlvried, H. Guo, Y. Wu, J. P. Golden, Y. Xue, J. G. Grajales-Reyes, X. Wang, S. Krishnan, Y. Xie, D. Peng, C.-J. Su, F. Zhang, J. T. Reeder, S. K. Vogt, Y. Huang, J. A. Rogers, R. W. Gereau, *Sci. Adv.* **2019**, *5*, eaaw5296.

[34] Y. S. Choi, Y. Y. Hsueh, J. Koo, Q. Yang, R. Avila, B. Hu, Z. Xie, G. Lee, Z. Ning, C. Liu, Y. Xu, Y. J. Lee, W. Zhao, J. Fang, Y. Deng, S. M. Lee, A. Vázquez-Guardado, I. Stepien, Y. Yan, J. W. Song, C. Haney, Y. S. Oh, W. Liu, H. J. Yun, A. Banks, M. R.

MacEwan, G. A. Ameer, W. Z. Ray, Y. Huang, T. Xie, C. K. Franz, S. Li, J. A. Rogers, *Nat. Commun.* **2020**, *11*, 5990.

[35] J. Koo, M. R. MacEwan, S.-K. Kang, S. M. Won, M. Stephen, P. Gamble, Z. Xie, Y. Yan, Y.-Y. Chen, J. Shin, N. Birenbaum, S. Chung, S. B. Kim, J. Khalifeh, D. V Harburg, K. Bean, M. Paskett, J. Kim, Z. S. Zohny, S. M. Lee, R. Zhang, K. Luo, B. Ji, A. Banks, H. M. Lee, Y. Huang, W. Z. Ray, J. A. Rogers, *Nat. Med.* **2018**, *24*, 1830.

[36] D. M. Ackermann, E. L. Foldes, N. Bhadra, K. L. Kilgore, *J. Neurosci. Methods* **2010**, *193*, 72.

[37] G. H. Borschel, K. F. Kia, W. M. J. Kuzon, R. G. Dennis, *J. Surg. Res.* **2003**, *114*, 133.

[38] M.-S. JU, C.-C. K. LIN, C.-T. CHANG, *J. Biomech. Sci. Eng.* **2017**, *12*, 16.

[39] J. H. Fan, W. I. Hung, W. T. Li, J. M. Yeh, in *IFMBE Proc.* (Eds.: C.T. Lim, J.C.H. Goh), Springer Berlin Heidelberg, Berlin, Heidelberg, **2009**, pp. 870–873.

[40] D. Krakauer, *Analog Dialogue* **2006**, *40*, 1.

[41] Z. Suo, *MRS Bull.* **2012**, *37*, 218.

[42] J. A. Fan, W.-H. Yeo, Y. Su, Y. Hattori, W. Lee, S.-Y. Jung, Y. Zhang, Z. Liu, H. Cheng, L. Falgout, M. Bajema, T. Coleman, D. Gregoire, R. J. Larsen, Y. Huang, J. A. Rogers, *Nat. Commun.* **2014**, *5*, 3266.

[43] C. W. Baek, J. M. Kim, Y. K. Kim, J. H. Kim, H. J. Lee, S. W. Han, *Sensors Mater.* **2005**, *17*, 277.

[44] B. Putz, R. L. Schoeppner, O. Glushko, D. F. Bahr, M. J. Cordill, *Scr. Mater.* **2015**, *102*, 23.

[45] R. S. Figliola, D. E. Beasley, *Meas. Sci. Technol.* **1996**, *7*.

[46] B. J. Pfister, T. Gordon, J. R. Loverde, A. S. Kochar, S. E. Mackinnon, D. K. Cullen, *Crit. Rev. Biomed. Eng.* **2011**, *39*, 81.

[47] S. Türedi, E. Yuluğ, A. Alver, A. Bodur, İ. İnce, *Exp. Ther. Med.* **2018**, *15*, 3215.

[48] E. A. E. Van Tienhoven, D. Korbee, L. Schipper, H. W. Verharen, W. H. De Jong, *J. Biomed. Mater. Res. Part A* **2006**, *78A*, 175.

[49] J. Koo, S. B. Kim, Y. S. Choi, Z. Xie, A. J. Bandodkar, J. Khalifeh, Y. Yan, H. Kim, M. K. Pezhouh, K. Doty, G. Lee, Y. Y. Chen, S. M. Lee, D. D'Andrea, K. Jung, K. H. Lee, K. Li, S. Jo, H. Wang, J. H. Kim, J. Kim, S. G. Choi, W. J. Jang, Y. S. Oh, I. Park, S. S. Kwak, J. H. Park, D. Hong, X. Feng, C. H. Lee, A. Banks, C. Leal, H. M. Lee, Y. Huang, C. K. Franz, W. Z. Ray, M. MacEwan, S. K. Kang, J. A. Rogers, *Sci. Adv.* **2020**, *6*.